High-temperature electron transport in metamorphic InGaAs/InAlAs heterostructures

T. Suzuki[1*], H. Ono[2], and S. Taniguchi[2]

[1] *Center for Nano Materials and Technology, Japan Advanced Institute of Science and Technology 1-1 Asahidai, Nomi-shi, Ishikawa, 923-1292, Japan*

[2] *Advanced Devices R&D Department, Semiconductor Solutions Network Company, Sony Corporation 4-14-1 Asahi-cho, Atsugi-shi, Kanagawa, 243-0014 Japan*

Abstract

We have investigated high-temperature electron transport in metamorphic InGaAs/InAlAs modulation-doped heterostructures with several indium contents. The electron mobility characterizing the low-field transport properties was obtained from the Hall measurements. From room temperature to 400 K, ~ 26 % decrease in the mobility was observed, which is well-explained by the polar-optical-phonon scattering theory. The indium content dependence of the mobility is explained by the theory with the Γ-valley electron mass. On the other hand, the electron saturation velocity characterizing the high-field transport properties was studied by means of the delay-time analysis of the transistors with gate length of 0.12-1.0 μm. We observed ~ 12 % decrease in the saturation velocity from room temperature to 400 K, which is smaller than that in the mobility and roughly consistent with the energy relaxation theory. In the indium content dependence of the saturation velocity, the effect of decrease in the electron density in the L- and X-valley is important. The high-frequency performance of the transistors at high temperatures shows a deterioration according to the decrease in the saturation velocity.

Keywords— metamorphic InGaAs/InAlAs, electron mobility, electron saturation velocity, delay-time analysis, high-frequency performance

*Corresponding author. E-mail address: tosikazu@jaist.ac.jp; Phone:+81-761-51-1441; Fax:+81-761-51-1455 (T.Suzuki)

1 Introduction

Recently, semiconductor devices obtained from lattice-mismatched growth, called metamorphic growth, have received considerable attention. In the metamorphic growth, the lattice mismatch between active device layers and the substrate is relaxed by devised buffer layers. Since InGaAs with high indium content provides high electron mobility and saturation velocity, InGaAs devices obtained from the metamorphic growth on GaAs substrates, such as metamorphic high electron mobility transistors (MHEMTs)[1,2] and metamorphic heterojunction bipolar transistors (MHBTs)[3,4], are attractive for high-frequency or high-speed applications. In addition to the fact that the metamorphic InGaAs devices have a cost advantage in comparison with lattice-matched InGaAs devices grown on InP substrates, it is important that the metamorphic devices offer a freedom of choice of the indium content. As the metamorphic growth enables us to realize an unstrained InGaAs layer with almost any indium content, the indium content is considered as a new structure parameter in the device design; high-frequency performance and breakdown voltage can be balanced by choosing the indium content in device optimization[5,6].

For further development of the narrow-bandgap InGaAs metamorphic devices, deterioration in the device performance at high temperatures is an important issue for practical use. In this work, in order to elucidate the deterioration, we have investigated high-temperature electron transport properties in the metamorphic InGaAs/InAlAs heterostructures grown on GaAs substrates with several indium contents, in comparison with the lattice-matched heterostructures grown on InP substrates. The low-field transport properties have been studied through characterization of the electron mobility obtained from the Hall measurements up to 400 K, in

comparison with polar-optical-phonon and alloy-disorder scattering theory. On the other hand, the high-field transport properties have been investigated by means of high-frequency measurements of the transistors with gate length of 0.12-1.0 μm up to 473 K. The high-temperature electron saturation velocity obtained from the delay-time analysis is compared with the energy relaxation theory.

2 Materials

The modulation-doped metamorphic $In_xGa_{1-x}As/In_xAl_{1-x}As$ heterostructures ($x = 0.36$, 0.43, and 0.53) were grown on semi-insulating (001)GaAs substrates by means of molecular beam epitaxy. Following the undoped graded InAlAs metamorphic buffer layer, the active layers incorporated 200 nm undoped InAlAs layer, 15 nm undoped InGaAs quantum-well channel, 6 nm undoped InAlAs spacer, Si delta-doping plane, 12 nm undoped InAlAs barrier layer, and 50 nm n^+-InGaAs cap layer. The lattice-matched (LM) $In_{0.53}Ga_{0.47}As/In_{0.52}Al_{0.48}As$ heterostructures grown on InP have the same active layers. The indium contents were precisely determined by photoluminescence measurements taking into account quantized energy levels in the channels, and (004) and (115) X-ray diffraction measurements.

In the metamorphic growth, surface with crosshatch is obtained. Figure 1 shows, as an example, the atomic force microscope (AFM) image of the heterostructure with the indium content of 0.43. The root mean square roughness of the metamorphic materials is as large as $\sim$ 2-3 nm. From plan-view transmission electron microscope (PTEM) observation, as shown in Fig. 2, we have found rather high-density crystalline defects, threading dislocations and stacking faults, in the active layers of metamorphic heterostructures. The defect density was

typically on the order of 10^8 cm^{-2}, which is larger than the case of LM structures by three orders of magnitude. It should be noted that the defect density cannot be estimated from cross-sectional TEM (XTEM) observations, especially for the metamorphic materials with defect density $\lesssim 10^8$ cm^{-2}[7], because it seems as if almost all dislocations were confined inside the buffer layer from the XTEM observation. At the present time, even in the best case, we observe the defects on the order of 10^7 cm^{-2} in the active layer of the metamorphic devices. Although there are some reports which conclude that the defect density in InGaAs MHEMTs or MHBTs is $\lesssim 10^6$ cm^{-2} from XTEM observations, we consider that they are underestimated results. In spite of the surface roughness and the high-density defects, as shown below, we obtain the same electron transport properties of the metamorphic structure with $x = 0.53$ and the LM structure, which indicates that the effects of the surface roughness and defects on the transport properties are negligible.

3 Electron mobility

We have carried out Hall measurements (van der Pauw method) of the heterostructures after recess etching up to 400 K. For all the heterostructures, the sheet carrier (electron) concentration is $\sim 3.5 \times 10^{12}$ cm^{-2}, which is almost constant up to 400 K. Figure 3 shows the temperature dependence of the electron mobility μ obtained from the Hall measurements. We obtain the mobility at room temperature (295 K) of $\mu = 8100$, 8900, and 10300 cm^2/Vs for $x = 0.36$, 0.43, and 0.53, respectively. The same temperature dependence is obtained for the metamorphic structure with x=0.53 and the LM structure. This indicates that the defects do not affect the mobility. In the region higher than room temperature, the most dominant mechanism limiting

the low-field mobility is polar-optical-phonon scattering[8], which gives the mobility as a function of temperature T,

$$\mu_{\rm pop} = \frac{3\sqrt{2\pi^3}\hbar^2}{e{m^*}^{3/2}{E_{\rm op}}^{1/2}} \left(\frac{1}{\epsilon_\infty} - \frac{1}{\epsilon}\right)^{-1} \frac{\exp\left(E_{\rm op}/k_{\rm B}T\right) - 1}{(E_{\rm op}/k_{\rm B}T)^{3/2}\ \exp\left(E_{\rm op}/2k_{\rm B}T\right)\ K_1(E_{\rm op}/2k_{\rm B}T)}, \quad (1)$$

where m^* is the electron effective mass, $E_{\rm op}$ is the optical phonon energy, ϵ_∞ and ϵ are the high-frequency and static dielectric constants, and K_1 is a modified Bessel function. This formula is originally obtained for three-dimensional electron systems. However, in the case of the polar-optical-phonon scattering, the three-dimensional approach is justifiable also for two-dimensional electron systems as discussed in[9]. Therefore, the formula is valid for our InGaAs quantum-well channels. Assuming $m^* = m_\Gamma$, where $m_\Gamma = (0.067 - 0.0531x + 0.0091x^2)m_0$ is the InGaAs Γ-valley electron effective mass[10], and $E_{\rm op} \sim 35$ meV, we can estimate $\mu_{\rm pop} \lesssim 10^4$ cm^2/Vs in the high-temperature region, which is consistent with the measurements. In order to confirm that this scattering mechanism dominates the measured electron mobility, we investigate the normalized electron mobility, i.e., the mobility divided by the room-temperature mobility. Figure 4 shows measured temperature dependence of the normalized mobility and the theoretical curve obtained from (1) assuming $E_{\rm op} = 35$ meV. We find universal behavior of the normalized mobility for every indium contents in quite good agreement with the theory. From room temperature to 400 K, approximately 26 % decrease in the mobility is observed according to the enhanced polar-optical-phonon scattering.

The other important scattering mechanism is the alloy-disorder scattering[11], which gives

almost temperature independent mobility

$$\mu_{\rm alloy} = \frac{\pi e \hbar^4}{\sqrt{2}x(1-x)m^{*5/2}\Omega V^2 {E_{\rm F}}^{1/2}}, \tag{2}$$

where Ω is the unit cell volume, V is the alloy-disorder potential, and $E_{\rm F}$ is the Fermi energy. We can estimate $\mu_{\rm alloy} \gtrsim 10^5$ cm^2/Vs, where we use $V \sim 0.5$ eV[12] and $E_{\rm F} \sim 100$ meV for our structures. Although the theory is for the three-dimensional case and should be slightly modified for the two-dimensional case, the order estimation is unchanged. Therefore, we can conclude that the alloy-disorder scattering gives only small correction of the mobility.

The indium content dependence of the electron mobility should be well-described through m_Γ dependence of the mobility, according to the polar-optical-phonon scattering given by (1). In fact, as shown in Fig. 5, the measured room-temperature mobility is proportional to $1/{m_\Gamma}^{3/2}$. This clearly shows that the mobility increase with increasing in the indium content is according to the reduction of m_Γ.

4 Electron saturation velocity

In order to examine the electron saturation velocity, we fabricated T-gate transistors with gate length of 0.12-1.0 μm according to the following device process[6,13]. The fabrication was started with isolation by wet etching. The T-gate structures were realized by tri-layer resist process with electron-beam lithography. The gate length was precisely measured by using a critical dimension scanning electron microscope. After the recess etching, Pt/Ti/Pt/Au was deposited and lifted-off for the gate. Then alloyed Ni/AuGe/Au ohmic contacts were formed. Typically, the ohmic contact resistance was 0.35, 0.3, and 0.2 Ωmm for x=0.36, 0.43, and 0.53, respectively. Finally,

Ti/Au contact pads were formed. The current gain cut-off frequency f_{T} of the transistors was measured at high temperatures up to 473 K. From the gate length L_{g} dependence of current gain cut-off frequency f_{T} at room temperature, $L_{\mathrm{g}} \times f_{\mathrm{T}}$ of 23, 27, and 32 GHz·μm is obtained for the $x = 0.36$, 0.43, and 0.53, respectively.

In order to investigate electron saturation velocity, we performed the delay-time analysis[14]. The total delay time $\tau = 1/2\pi f_{\mathrm{T}}$ is divided into two parts, the channel charging time, which is proportional to the reciprocal drain current density, and the saturation velocity transit time, during which electrons with the saturation velocity transit under the gate. Therefore, the saturation velocity transit time can be obtained from the extrapolation of the total delay time at infinite drain current density. Figure 6 shows the relation between the total delay time τ and the reciprocal drain current density $1/I_{\mathrm{d}}$ at room temperature, for the 1.0-μm-gate-length transistors. From the linear extrapolation of these plots, we can obtain the saturation velocity transit time τ_0. Figure 7 shows L_{g} dependence of τ_0 at room temperature. The electron saturation velocity v_{sat} at high electric fields $\gtrsim$ 10 kV/cm is evaluated from the slopes of these plots. At room temperature, we obtain $v_{\mathrm{sat}} = 1.8 \times 10^7$, 2.0×10^7, and 2.5×10^7 cm/s, for $x = 0.36$, 0.43, and 0.53, respectively. The same analysis for high temperatures gives the electron saturation velocity at high temperatures.

Figure 8 shows temperature dependence of the obtained saturation velocity. We obtained the same temperature dependence for the metamorphic structure with x=0.53 and the LM structure. This indicates that the defects do not affect the electron velocity at the high electric

fields. The saturation velocity is given by

$$v_{\rm sat} = \frac{2\sqrt{2}{E_{\rm op}}^{1/2}}{\sqrt{3\pi}{m^*}^{1/2}} \left[\frac{\exp\left(E_{\rm op}/k_{\rm B}T\right)-1}{\exp\left(E_{\rm op}/k_{\rm B}T\right)+1}\right]^{1/2} \tag{3}$$

from the energy relaxation theory[15]. Since the theory is based on the polar-optical-phonon scattering, it is valid for both two- and three-dimensional electron systems. In order to compare the measured results and the theory, we plot the normalized saturation velocity, i.e., the saturation velocity divided by the room-temperature saturation velocity, in Fig. 9. The solid curve is the theoretical value obtained from (3) assuming $E_{\rm op}$ of 35 meV. Although $v_{\rm sat}$ for higher indium contents exhibits deviations from theoretical values at higher temperatures, we find the measurements are roughly consistent with the theory. We observe approximately 12 % decrease in the saturation velocity from room temperature to 400 K, in contrast with the 26 % decrease in the mobility. From room temperature to 473 K, we observe $\sim$ 19 % decrease in the saturation velocity for $x = 0.36$, which is in agreement with the theory. However, for $x = 0.43$ and $x = 0.53$, $\sim$ 23 % decrease in the saturation velocity is observed, which is slightly larger than the theoretical value.

It should be noted that, the electron effective mass m^* in (3) is the average electron effective mass based on the electron distribution in several valleys contributing the high-field transport. From the measured saturation velocity, we can estimate the average electron effective mass. In Fig. 10, we show the average electron effective mass estimated from the measurements comparing with m_Γ. Although the average electron effective mass is rather large in the lower indium content region, it decreases rapidly with the increase in the indium content. As the energy separation between the Γ-valley and the upper (L- and X-) valleys increases with the increase in the indium

contents, the electron density in the upper valleys decreases and the velocity overshoot effects become important.

The high-frequency performance of the transistors at high temperatures shows a deterioration according to the decrease in the saturation velocity. Figure 11 shows the temperature dependence of $L_{\mathrm{g}} \times f_{\mathrm{T}}$. The decrease in the $L_{\mathrm{g}} \times f_{\mathrm{T}}$ is mainly due to the decrease in the saturation velocity.

5 Summary

In summary, we investigated electron transport properties in the InGaAs/InAlAs heterostructures at high temperatures. The low-field mobility and the high-field saturation velocity were discussed comparing with a theory. From room temperature to 400 K, we obtain approximately 26 % and 12 % decrease in the mobility and the saturation velocity, respectively. The high-frequency performance of the transistors at high temperatures shows a deterioration mainly due to the decrease in the saturation velocity.

Acknowledgments

The authors are grateful to Dr. S. Tomiya for analysis of the metamorphic materials. This work was supported by Center for Nano Materials and Technology (CNMT), Japan Advanced Institute of Science and Technology (JAIST).

References

[1] H. Masato, T. Matsuno, and K. Inoue, Jpn. J. Appl. Phys. **30** (1991) 3850.

[2] T. Mishima, K. Higuchi, M. Mori, and M. Kudo, J. Cryst. Growth **150** (1995) 1230.

[3] H. Q. Zheng, K. Radhakrishnan, H. Wang, K. H. Yuan, S. F. Yoon, and G. I. Ng, Appl. Phys. Lett. **77** (2000) 869.

[4] W. K. Liu, D. Lubyshev, Y. Wu, X. M. Fang, T. Yurasits, A. B. Cornfeld, D. Mensa , S. Jaganathan, R. Pullela, M. Dahlstrom, P. K. Sundararajan, T. Mathew, and M. Rodwell, Proc. 13th Int. Conf. on InP and Related Materials (2001) 284.

[5] Y. Cordier, S. Bollaert, M. Zaknoune, J. diPersio, and D. Ferre, Proc. 10th Int. Conf. on InP and Related Materials (1998) 211.

[6] H. Ono, S. Taniguchi, and T. Suzuki, Jpn. J. Appl. Phys. **43** (2004) 2259.

[7] M. T. Bulsara, C. Leitz, and E. A. Fitzgerald, Appl. Phys. Lett. **72** (1998) 1608.

[8] K. Seeger, *Semiconductor Physics* (Springer-Verlag, 1999) p. 208.

[9] W. Walukiewicz, H. E. Ruda, J. Lagowski, and H. C. Gatos, Phys. Rev. **B30**, (1984) 4571.

[10] I. Vurgaftman, J. R. Meyer, and L. R Ram-Mohan, J. Appl. Phys. **89** (2001) 5815.

[11] B. K. Ridley, *Quantum Process in Semiconductors* (Oxford Univ. Press, 1999) p. 181.

[12] S. Adachi, *Physical Properties of III-V Semiconductor Compounds* (John Wiley & Sons, 1992) p. 230.

[13] H. Ono, S. Taniguchi, and T. Suzuki, Proc. 16th Int. Conf. on InP and Related Materials (2004) 288.

[14] T. Enoki, K. Arai, and Y. Ishii, IEEE Electron Device Lett. **11** (1990) 502.

[15] P. A. Houston and A. G. R. Evans, Solid-State Electron. **20** (1977) 197.

Figure Captions

Figure 1

Atomic force microscope image of the surface of the metamorphic structure with indium content of 0.43. A surface with crosshatch is observed.

Figure 2

Plan-view transmission electron microscope image for the metamorphic structure with indium content of 0.43. High-density crystalline defects, threading dislocations and stacking faults, in the active layer are observed.

Figure 3

Temperature dependence of the electron mobility in the metamorphic InGaAs/InAlAs heterostructures.

Figure 4

Temperature dependence of the normalized electron mobility in comparison with the theory of the polar-optical-phonon scattering.

Figure 5

Relation between the room-temperature mobility and Γ-valley electron effective mass m_Γ. The mobility is proportional to $1/{m_\Gamma}^{3/2}$.

Figure 6

The total delay time $\tau = 1/2\pi f_\mathrm{T}$ as a function of the reciprocal drain current density $1/I_\mathrm{d}$ at room temperature for the 1.0-μm-gate-length transistors.

Figure 7

Saturation velocity transit time τ_0 as a function of the gate length L_g at room temperature.

Figure 8

Temperature dependence of the electron saturation velocity obtained from the delay-time analysis.

Figure 9

Temperature dependence of the normalized electron saturation velocity in comparison with the energy relaxation theory.

Figure 10

Indium content dependence of the average electron effective mass estimated from the saturation velocity, in comparison with the Γ-valley electron effective mass.

Figure 11

Temperature dependence of the $L_g \times f_T$. The high-frequency performance of the transistors at high temperatures shows a deterioration mainly due to the decrease in the saturation velocity.

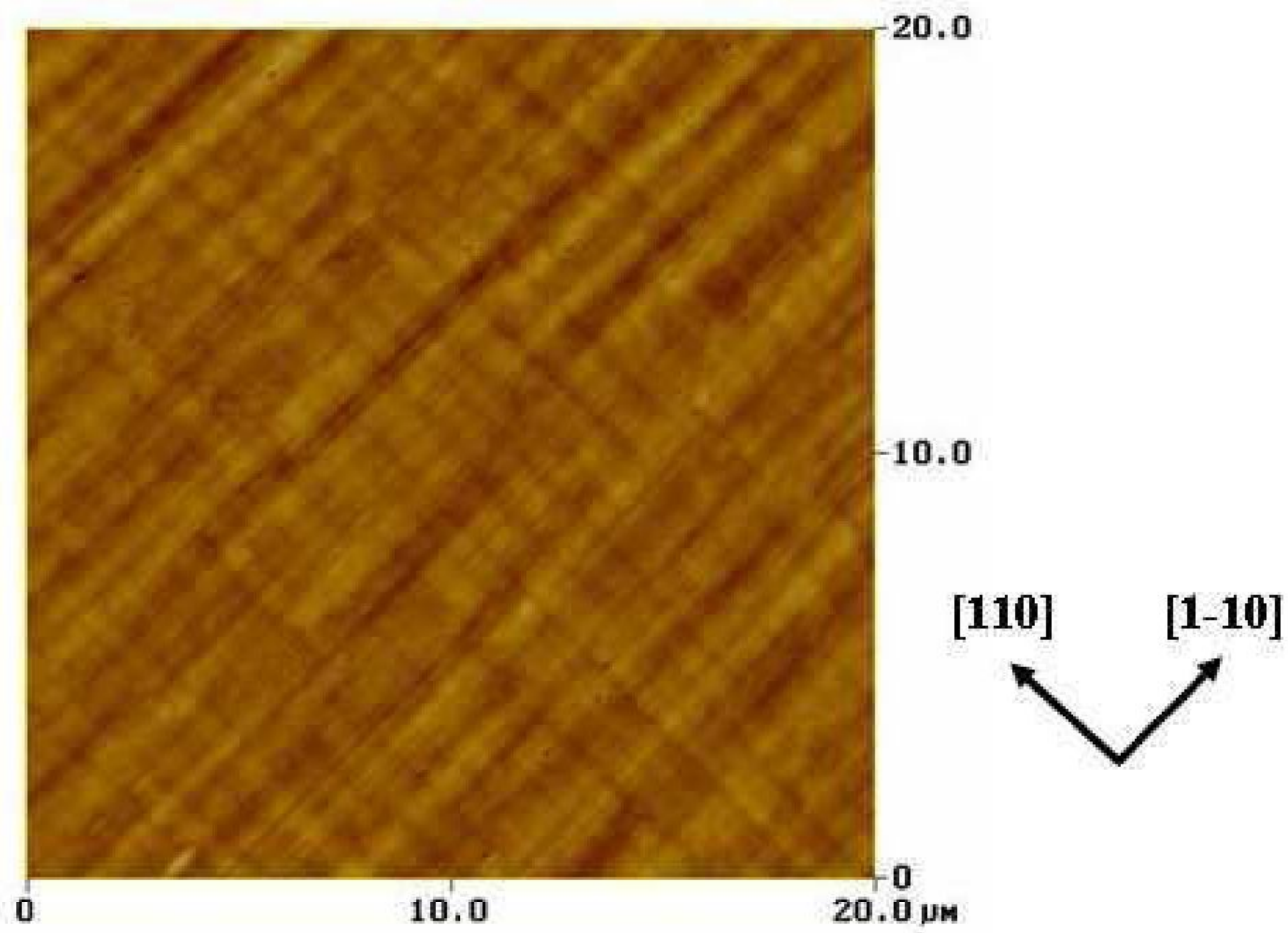

Fig. 1. T.Suzuki et al.

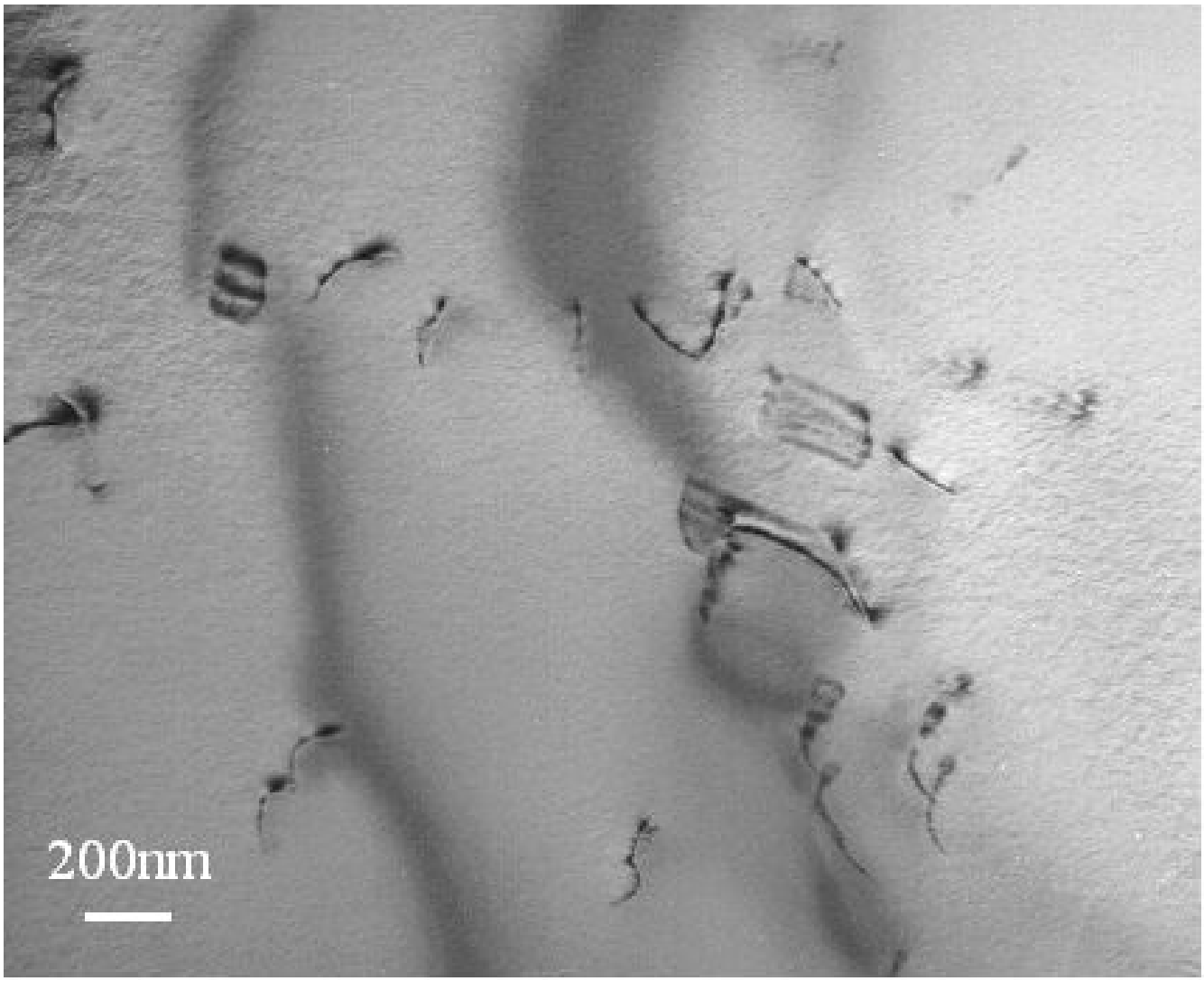

Fig. 2. T.Suzuki et al.

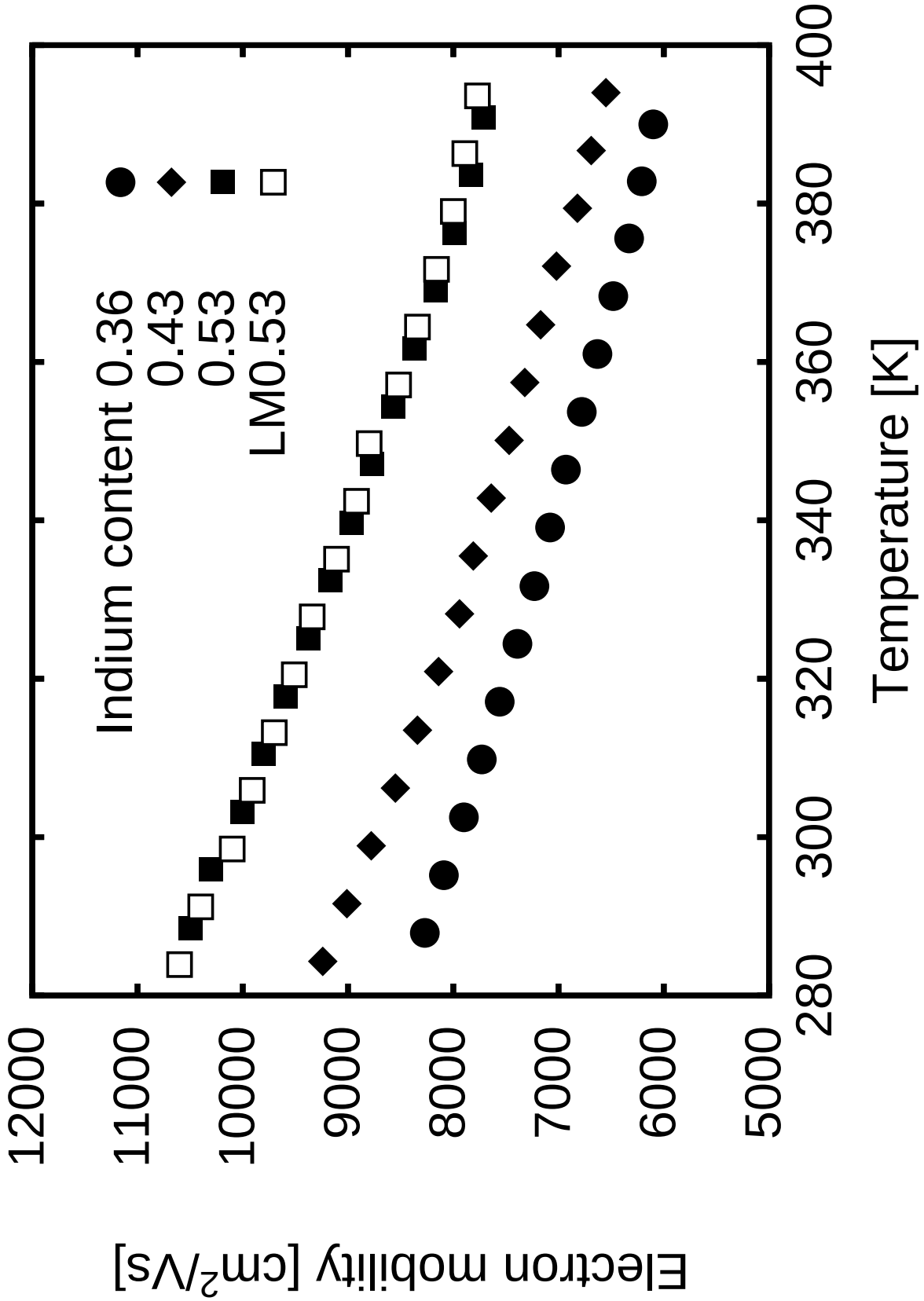

Fig. 3. T.Suzuki et al.

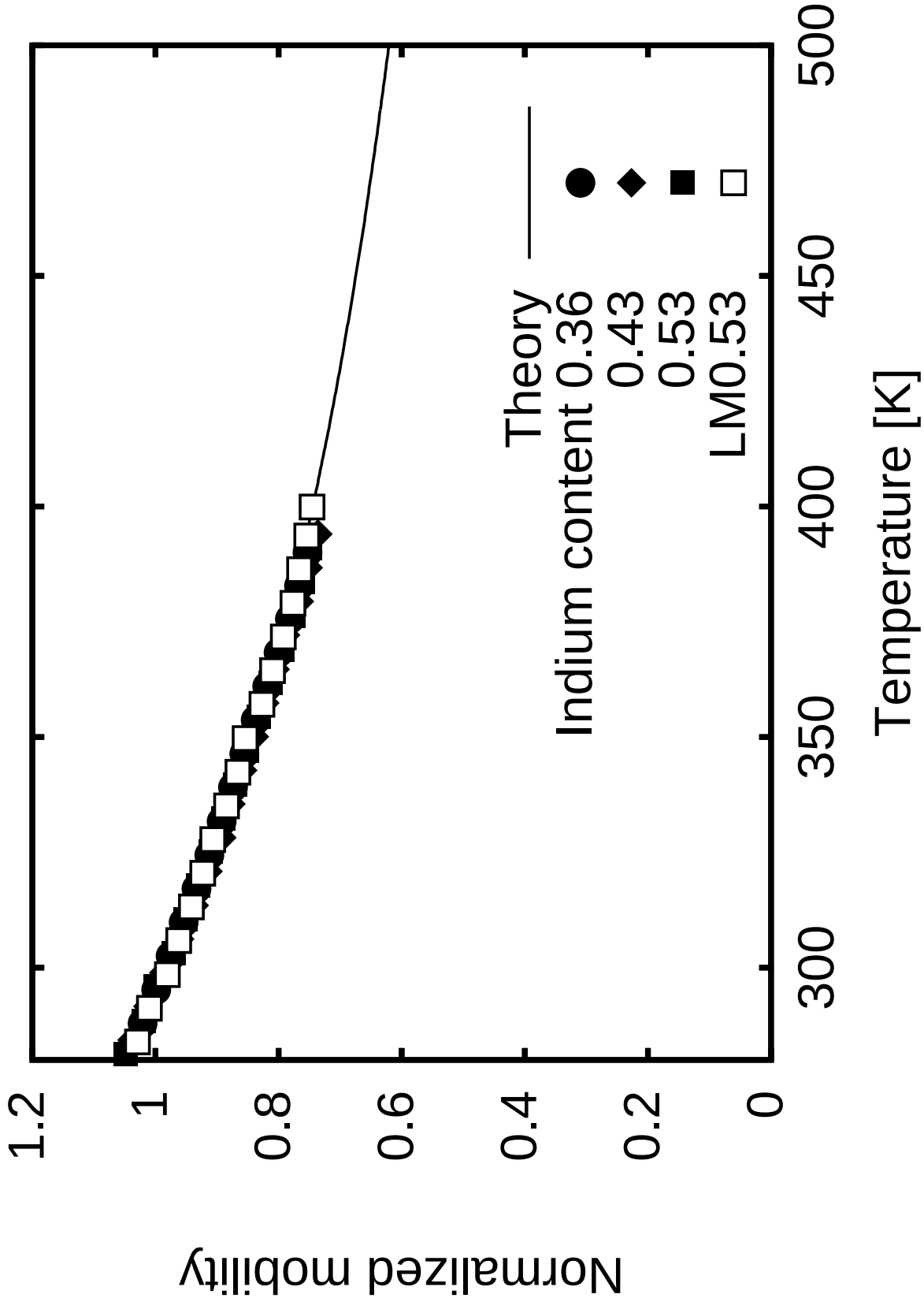

Fig. 4. T.Suzuki et al.

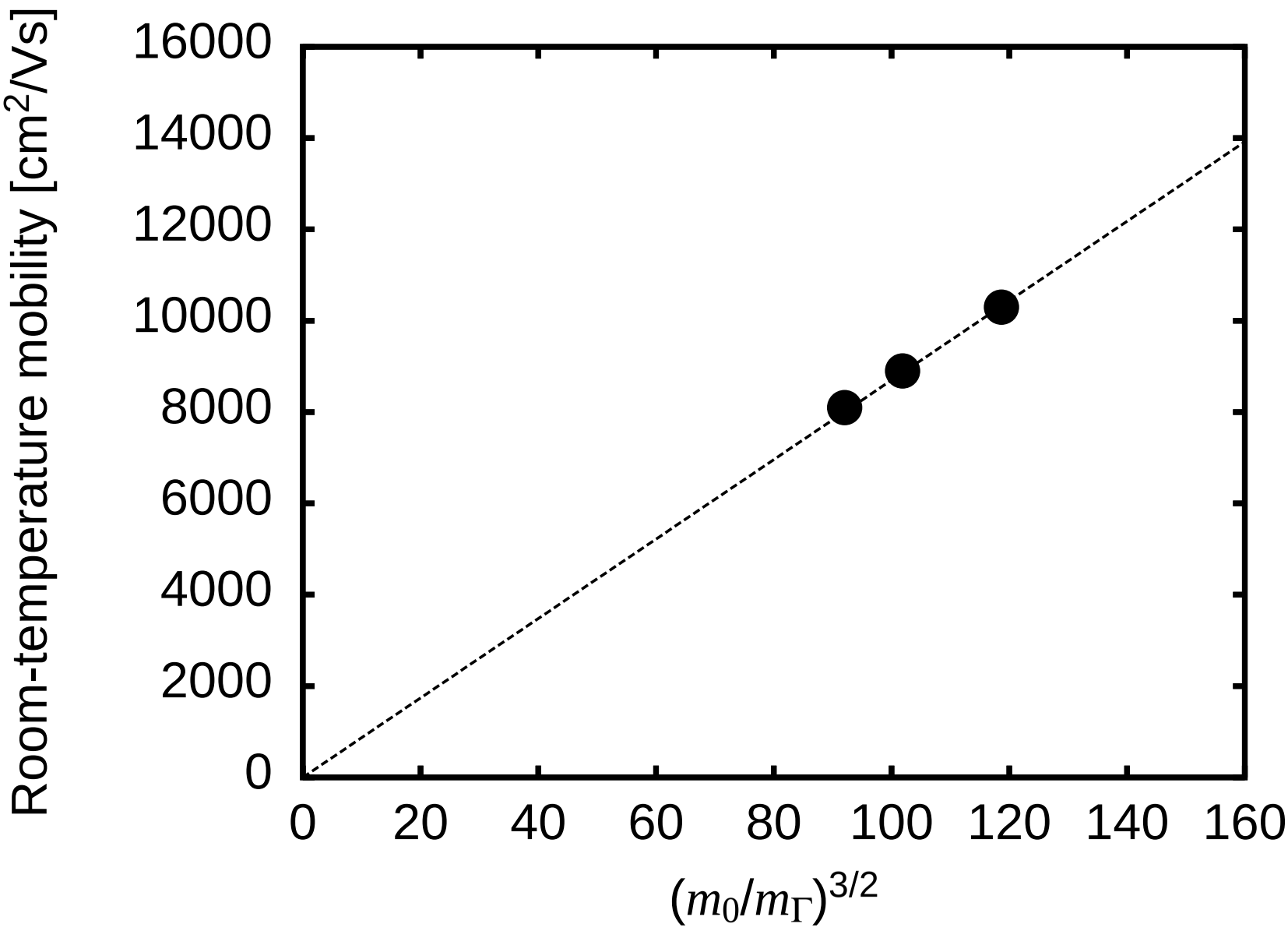

Fig. 5. T.Suzuki et al.

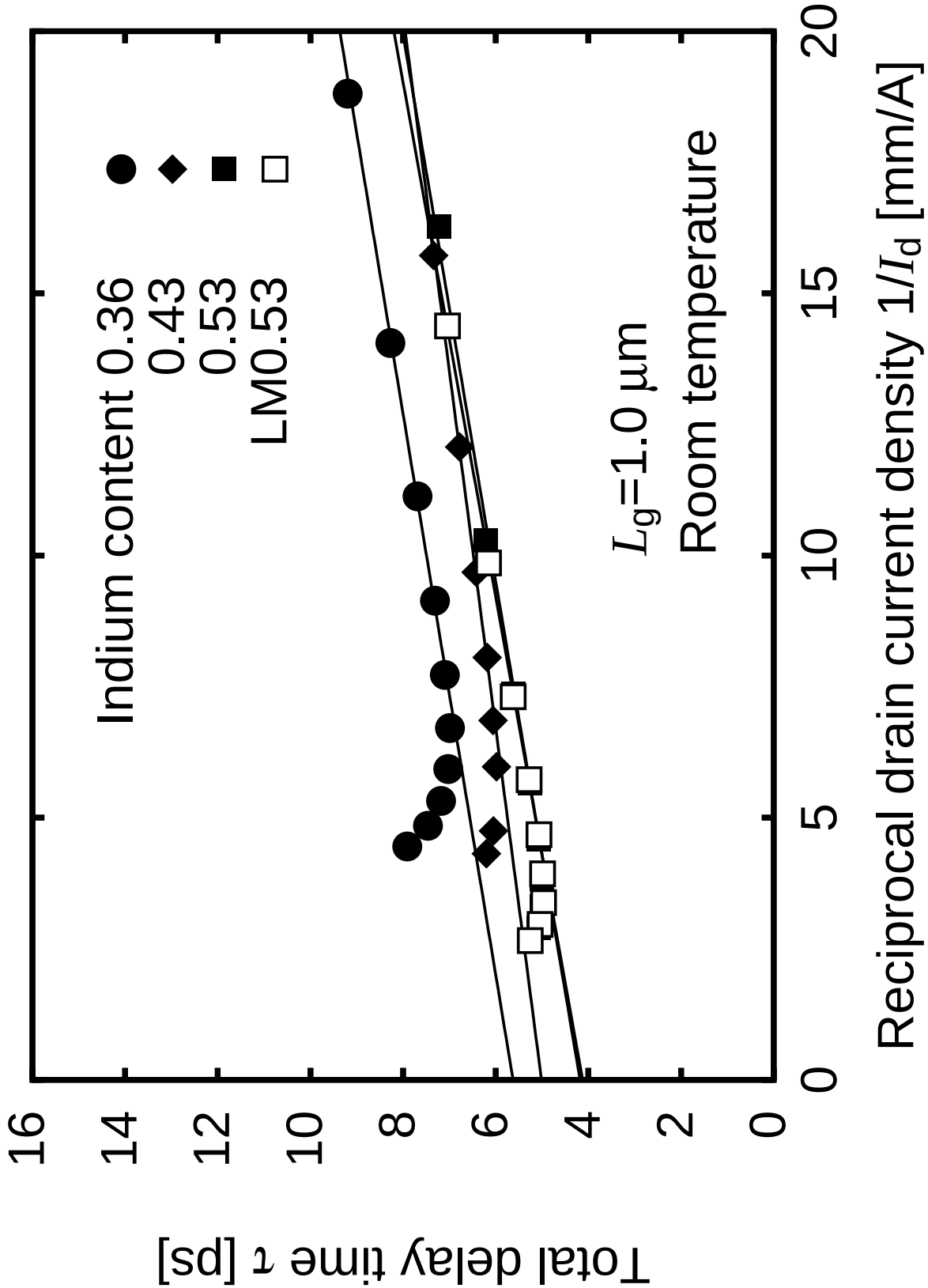

Fig. 6. T.Suzuki et al.

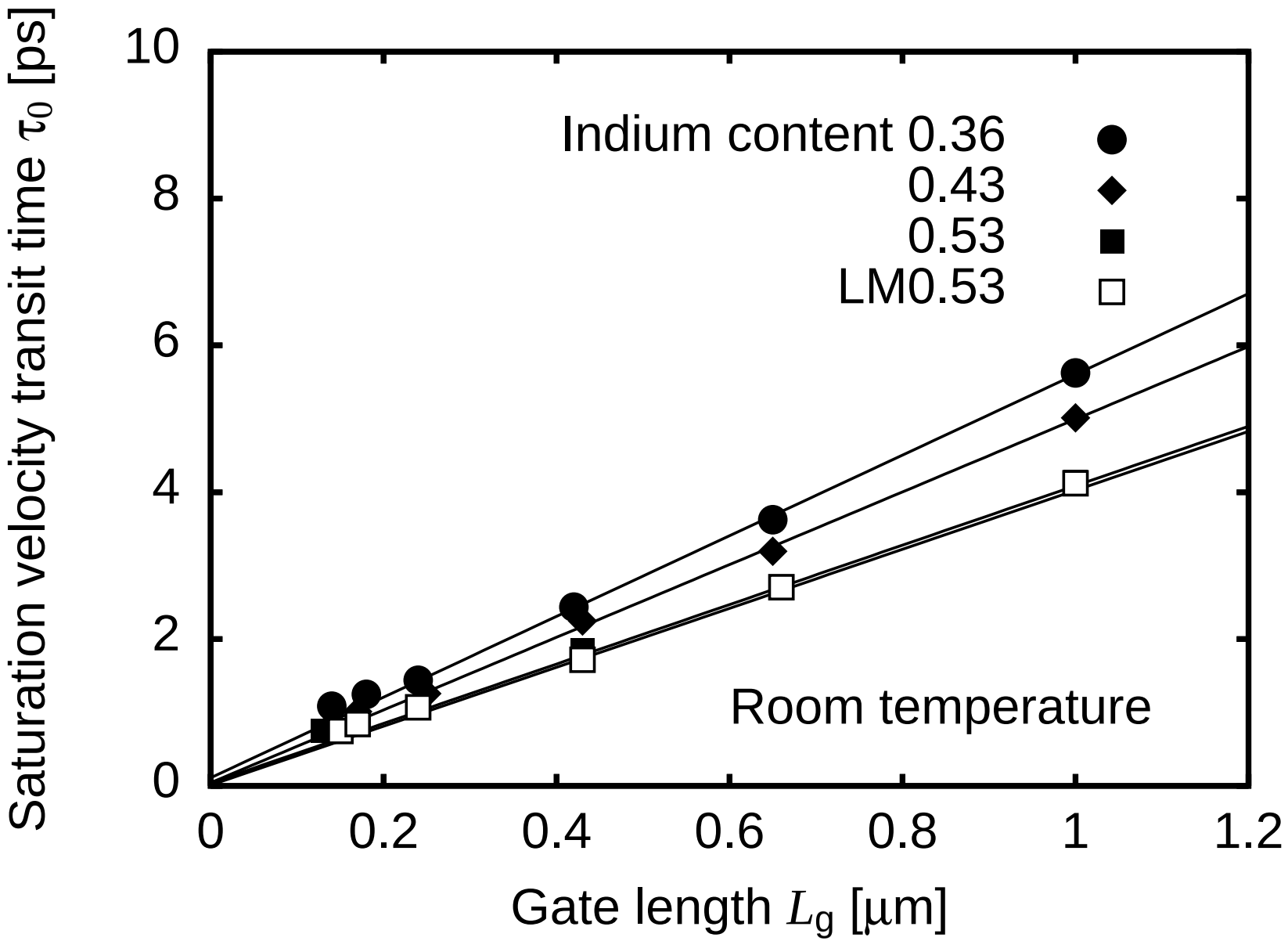

Fig. 7. T.Suzuki et al.

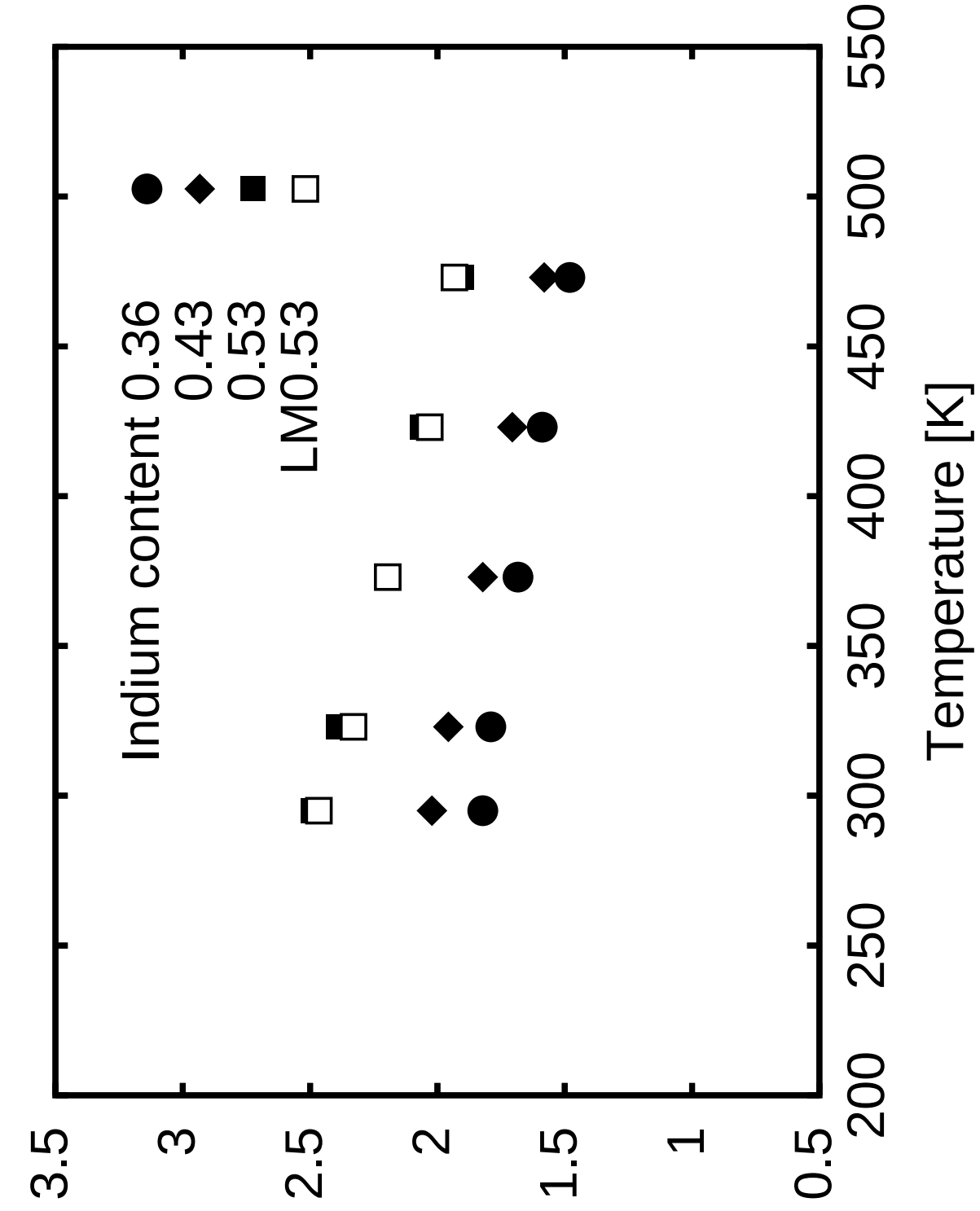

Fig. 8. T.Suzuki et al.

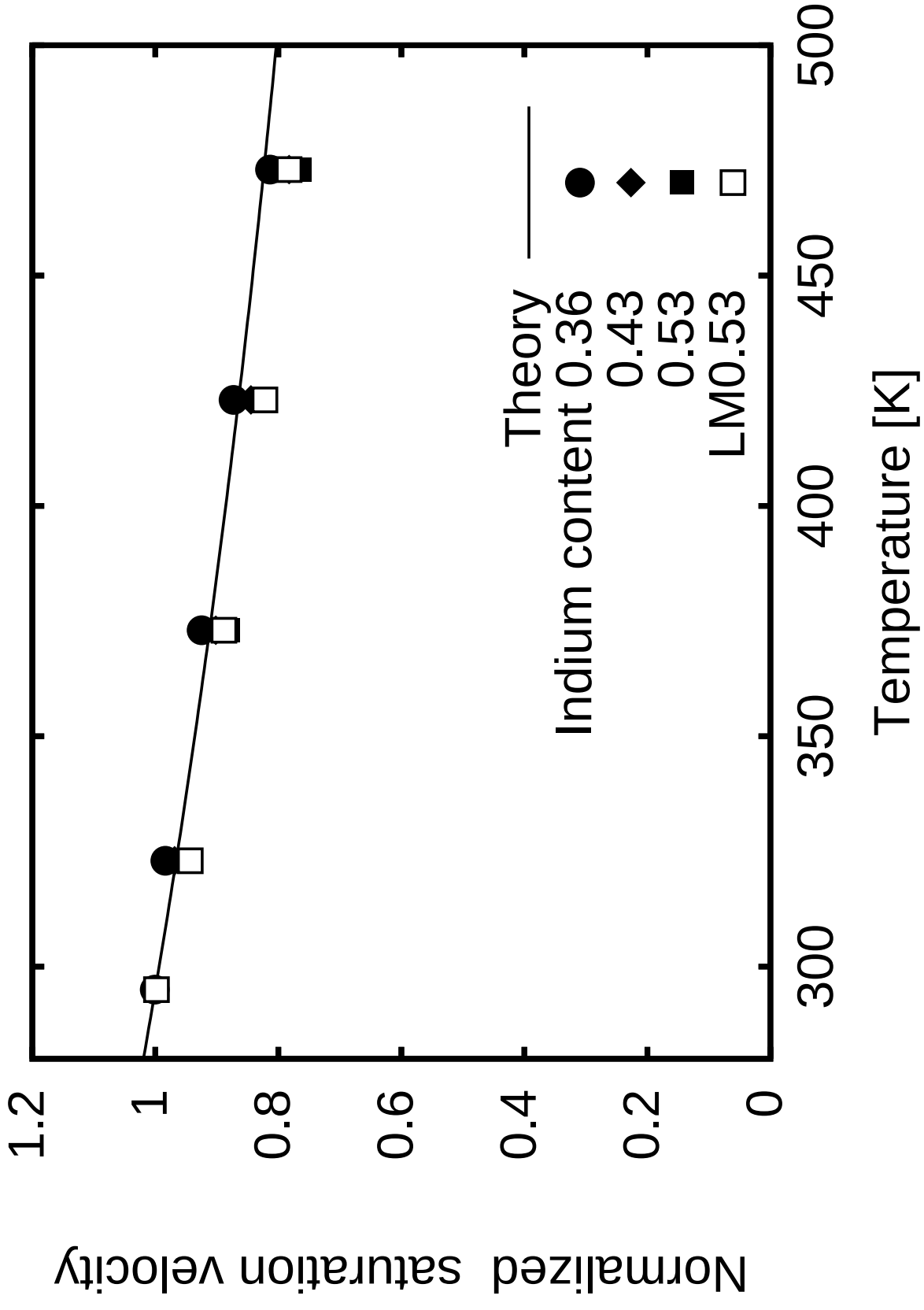

Fig. 9. T.Suzuki et al.

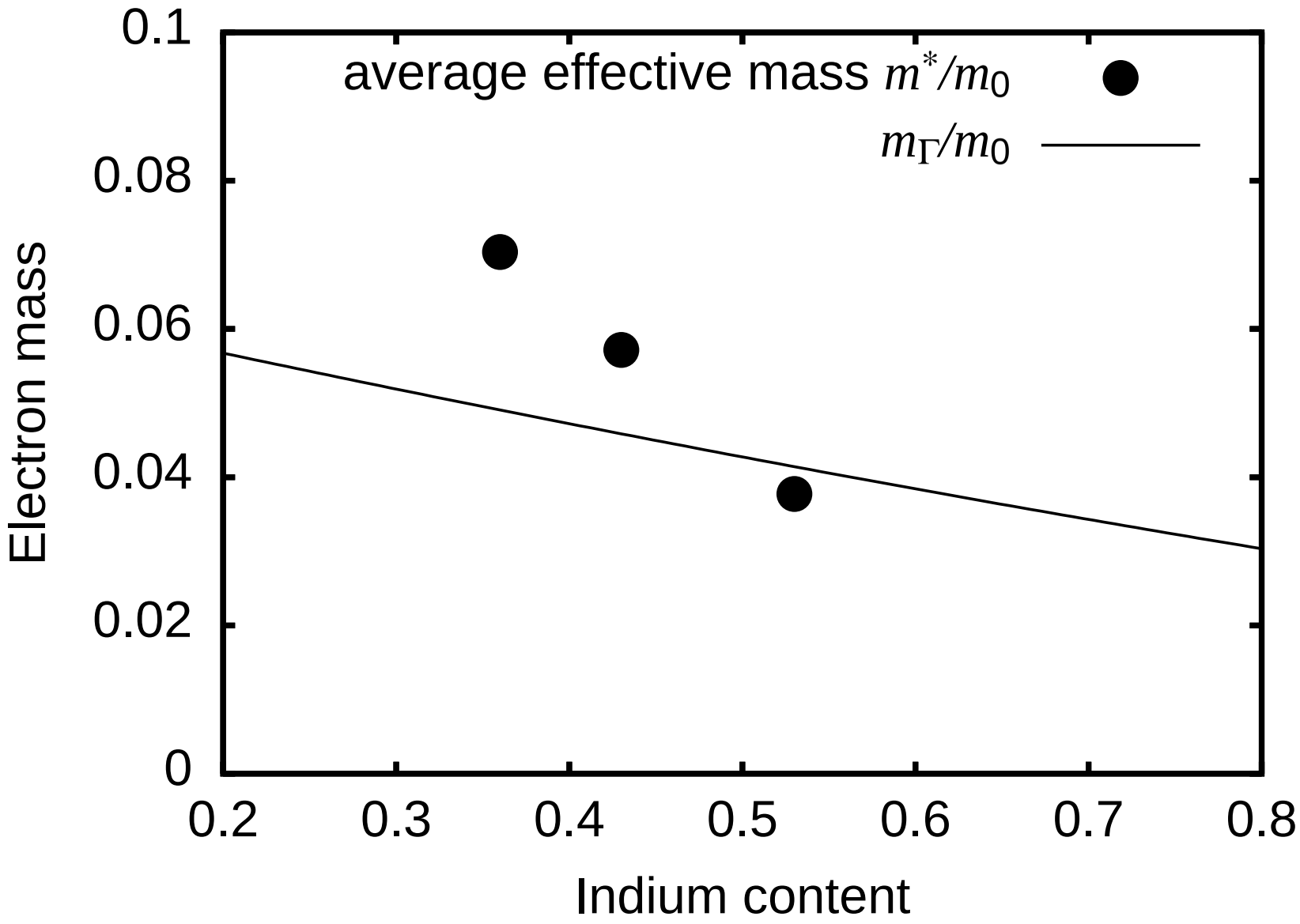

Fig. 10. T.Suzuki et al.

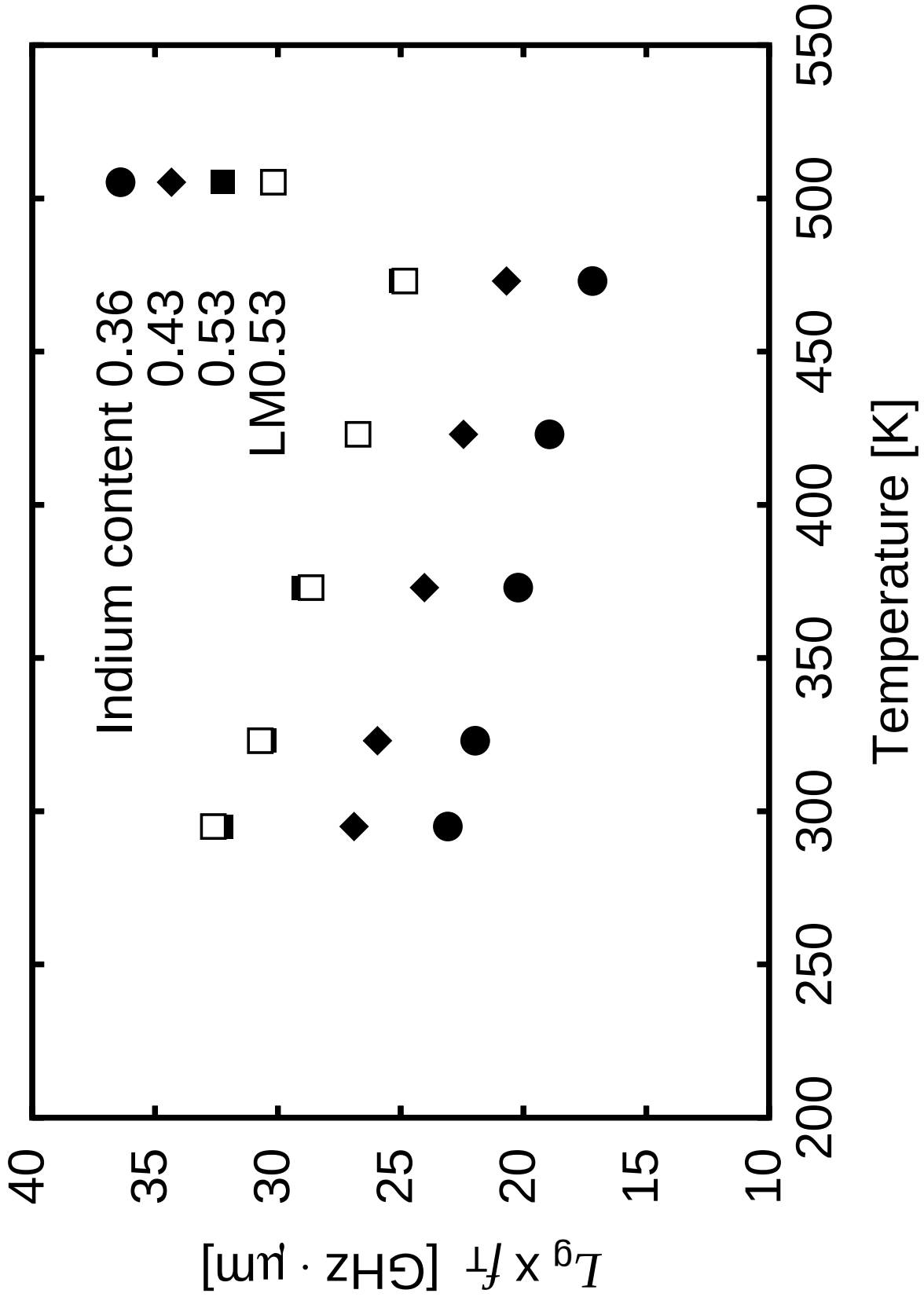

Fig. 11. T.Suzuki et al.